

Interband transitions and interference effects in superconducting qubits

Antti Paila · Jani Tuorila · Mika Sillanpää ·
David Gunnarsson · Jayanta Sarkar · Yuriy
Makhlin · Erkki Thuneberg · Pertti Hakonen

Received: date / Accepted: date

Abstract We investigate phase-sensitive interference effects in a periodically $\sin(2\pi f_{\text{rf}}t)$ -driven, artificial two-state system connected to a microwave resonator at $f_{LC} \simeq 800$ MHz. We observe two kinds of multiphoton transitions in the two-state system, accompanied by: 1) Several quanta from the drive at f_{rf} and 2) one quantum at f_{rf} and several at f_{LC} . The former are described using phase-sensitive Landau-Zener transitions, while the latter are discussed in terms of vibronic transitions in diatomic molecules. Interference effects in the vibronic transitions governed by Franck-Condon coefficients are also considered.

Keywords Landau-Zener tunneling · superconducting qubits · multiphoton transitions · Franck-Condon physics · Aharonov-Anandan phase

1 Introduction

Interference effects have been found to play an important role in the dynamics of qubits [1, 2, 3, 4, 5, 6]. For their understanding, the interference phenomena can be considered from different points of view: as interference between successive Landau-Zener (LZ) tunneling events [7, 8, 9], analogous to Mach-Zehnder interference [10], or in terms of spin dynamics [11]. In charge-phase qubits, strongly coupled to a microwave resonator,

This work was financially supported by the Academy of Finland, the Finnish Cultural Foundation, the Magnus Ehrnrooth Foundation, the Vaisala Foundation of the Finnish Academy of Science and Letters, EU-INTAS 05-1000008-7923, the Dynasty foundation, the presidential grant MD-4092.2007.2, and the EC-funded ULTI Project (Contract RITA-CT-2003-505313)

Antti Paila, Mika Sillanpää, David Gunnarsson, Jayanta Sarkar, and Pertti Hakonen
Low Temperature Laboratory, Helsinki University of Technology, FI-02015 TKK, Finland
Tel.: +358-9-4512964
Fax: +358-9-4512969
E-mail: pjh@boojum.hut.fi

Jani Tuorila and Erkki Thuneberg
Department of Physical Sciences, University of Oulu, FI-90014, Finland

Yuriy Makhlin
Landau Institute for Theoretical Physics, 119334 Moscow, Russia

analogy with vibrational transitions in diatomic molecules has been pointed out [12]. The fact that the latter phenomena are related to interference effects has its origin in the phase-space dynamics [13].

The state of a superconducting charge-phase qubit or a Cooper-pair box (CPB) can be monitored continuously by measuring its reactive response, either as an effective capacitance or inductance, which both are due to the curvature of the qubit's energy bands with respect to charge or phase degrees of freedom. When such a system is made as a part of an electric LC -oscillator circuit, any change of reactance, caused by the evolution of occupancies of the qubit's energy levels, will shift the resonance frequency of the resonator. This scheme has been used in several recent experiments, typically having the qubit, with splitting ΔE , connected to a coplanar stripline cavity near resonance [14]. We have, however, worked in the fully detuned limit where $f_{LC} \ll \Delta E/h$. At weak drive, such a read-out scheme perturbs the investigated system only weakly, allowing studies of inherent interference phenomena of the periodically driven two-level system.

We have investigated interference effects in the Cooper-pair box and in a charge-phase qubit circuit, configured as dual to the CPB (i.e., connected to the resonator via the phase, rather than the charge port), see Fig. 1. Both circuits provide good model systems of interference effects in periodically driven qubits. In the latter case, a clearly stronger coupling between the qubit and the resonator could be achieved, which made a difference in the observed effects.

The interference effects in these two circuits are diverse mostly due to the difference in the coupling between the resonator and the qubit. On the whole, interference phenomena can be understood in terms of multiphoton transitions. In strongly driven qubits, clear multiphoton transitions have been observed when the energy quantum of the rf-drive, multiplied by a small integer, matches the qubit level splitting [15,16]. In fact, multiphoton transitions allow a clear-cut distinction between our main findings. We may classify our observations as transitions where: 1) Several quanta from the drive at f_{rf} and 2) one quantum at f_{rf} and several at f_{LC} are exchanged between the qubit and its surrounding entities, i.e. the classical rf-drive port and the LC resonator. The first class can be treated as a sequence of phase-sensitive Landau-Zener transitions which produce a characteristic interference pattern, dependent on the "finesse" of the interferometer, namely the decoherence of the system. The latter class of transitions can be described in terms of vibronic transitions in diatomic molecules where potential changes are fast compared to the vibrational frequencies and non-adiabatic coupling between levels differing by a large number of quanta becomes possible. These phenomena include creation of several resonator quanta from the ground state, which is the non-adiabatic behavior referred to as the dynamical Casimir effect [17].

In this paper, we summarize some of our recent results [4,12] on interference effects in a driven superconducting charge qubit coupled to a resonator. The original references, in particular, used theoretical considerations and numerical simulations of the Bloch equations and the linear-response approximation for a detailed analysis of the shape of interference fringes when dissipation is important. Instead, here we try to concentrate on robust features which are amenable to general conclusions. For example, part of our analysis will be dealing with the phenomenon of destruction of tunneling.

The paper is organized as follows: First, we start with basics of the Cooper-pair box in Sect. 2 and describe the dynamics of a two-level system in Sect. 3, paying special attention to the destruction of tunneling from the ground state to the excited state. Sect. 4 covers our experimental work and results on CPBs, and it includes some

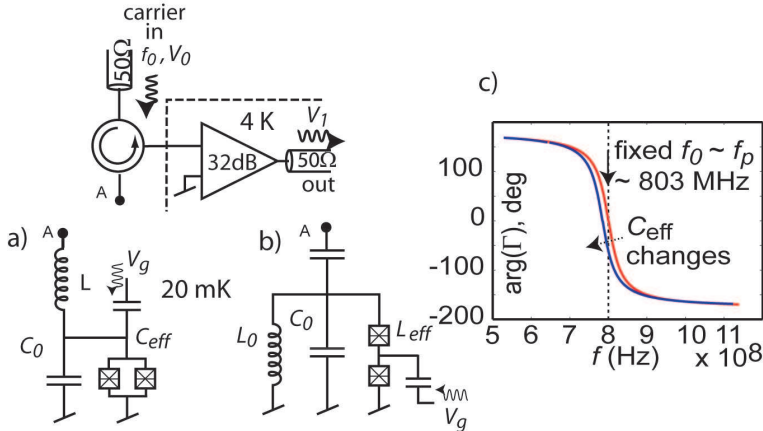


Fig. 1 Schematics of our experimental configurations: a) Cooper-pair box and b) the inductively read charge-phase qubit (LSET). In both configurations the qubit-induced change in the "quantum" reactance alters the resonant frequency $\omega_{LC}/2\pi$ of the tank circuit. This change causes a shift in phase of the reflected, constant-frequency microwave signal as illustrated in c). In the illustration, C_{eff} grows which leads to a reduction of ω_{LC} and, consequently, to a decrease of the reflection phase $\arg(\Gamma)$.

considerations aiming towards understanding of the Stokes phase and its relation to geometric phases in a spin-1/2 system. We present data at phase bias π (minimum band gap), and we analyze, especially, data in the regime of destruction of tunneling at the charge degeneracy. Results at zero phase bias can be found in Ref. [4]. Section 5 describes the analogy of spin flips in strongly coupled qubits with vibronic transitions in diatomic molecules. We do not describe much our experimental techniques, but to make the paper self-contained, we have explained some of the main technical points when presenting the experimental results.

2 Cooper-pair box

A split Cooper-pair box (CPB) is formed by a single-Cooper-pair transistor (SCPT) embedded into a small superconducting loop [18, 19, 20], see Fig. 1. The charging energy of the CPB, $E_c = e^2/2C_\Sigma \sim 1$ Kelvin, is given by the total capacitance C_Σ which includes the junction capacitances, the gate capacitance C_g , and the self-capacitance of the island. The effective Josephson energy is given by the sum of the energies of the individual junctions $(E_{J1} + E_{J2}) \cos(\phi/2) = E_J \cos(\phi/2)$, which is tunable by magnetic flux Φ , *i.e.* by the superconducting phase across the two junctions, $\phi = 2\pi\Phi/\Phi_0$. Here, $\Phi_0 = h/2e$ is the superconducting magnetic flux quantum.

We may write the Hamiltonian in the charge basis as

$$\hat{H} = \sum_n \left[E_c (\hat{n} - n_g)^2 |n\rangle\langle n| - \frac{E_J}{2} \cos \frac{\phi}{2} (|n-2\rangle\langle n| + |n+2\rangle\langle n|) + i \frac{E_J d}{2} \sin \frac{\phi}{2} (|n-2\rangle\langle n| - |n+2\rangle\langle n|) \right]. \quad (1)$$

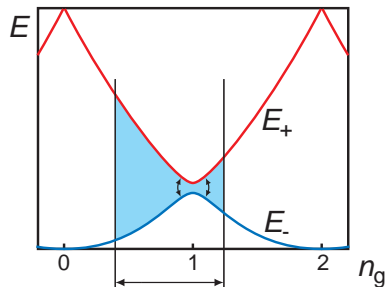


Fig. 2 The two lowest energy bands of Cooper-pair box as a function of the gate charge n_g (in units of e). In sweeping n_g (horizontal arrows), Landau-Zener tunneling between the bands takes place close to the point where the energy difference is at minimum (curved arrows). Successive sweeps can lead to interference of the tunneling events. The interference depends on the phase (6) accumulated in the shaded area.

Here \hat{n} denotes the number of extra electron charges on the island, and $n_g = C_g V_g / e$ is the charge in electron units induced by the gate voltage V_g on the gate capacitor with capacitance C_g . \hat{n} is conjugate to $\hat{\theta}/2$, where $\hat{\theta}$ is the superconducting phase on the island. The asymmetry of the two Josephson junctions of the CPB is described by $d = (E_{J1} - E_{J2})/E_J$.

By assuming that $E_c \gg E_J$ and that n_g is close to 1, one can reduce the circuit to a two-state system, with the Hamiltonian

$$\hat{H} = \frac{1}{2} \begin{pmatrix} -4E_c(1 - n_g) & -E_J[\cos(\phi/2) + id \sin(\phi/2)] \\ -E_J[\cos(\phi/2) - id \sin(\phi/2)] & 4E_c(1 - n_g) \end{pmatrix} \quad (2)$$

in the basis of the relevant charge states $|0\rangle$ and $|2\rangle$. When this energy operator is expressed as a linear combination of the Pauli matrices $\hat{H} = -\frac{1}{2}(B_z \hat{\sigma}_z + B_x \hat{\sigma}_x + B_y \hat{\sigma}_y)$, we get the magnetic field components as $B_z = 4E_c(1 - n_g)$, $B_x = E_J \cos(\phi/2)$ and $B_y = dE_J \sin(\phi/2)$. The energies of the two states as a function of n_g are illustrated in Fig. 2.

In the experiments $E_J = 0.6$ K and $d = 0.22$, which means that the magnitude for the off-diagonal components $|\Delta|$ ranged over 1.4–6.2 GHz [4]. The non-linear parametric capacitance, which has been the cornerstone of our interference studies, has been experimentally studied in Refs. [21, 22].

3 Landau-Zener interference

We study the effect of sweeping the gate charge n_g . We denote the energy eigenstates by $|-\rangle$ and $|+\rangle$, and suppose the system is initially in the lower energy state $|-\rangle$, see Fig. 2. Two cases can be distinguished. When the sweep rate is small compared to the energy level difference, the system stays in the lower state. The alternative case is that the sweep rate is comparable to the level spacing. This may take place close to the degeneracy points, where the energy bands would cross in the absence of the Josephson coupling. There the system can tunnel from the lower state to the upper in a process known as Landau-Zener tunneling. The tunneling probability in a single

sweep is given by [7,8,9,11]

$$P_{LZ} = e^{-2\pi\gamma}, \quad \gamma = \frac{2\pi}{h} \frac{\Delta^2}{v}. \quad (3)$$

Here v is the speed at which the sweep passes the crossing point $v = |d(\epsilon_0 - \epsilon_2)/dt|$ and $\epsilon_0 - \epsilon_2 = 4E_c(1 - n_g)$ is the energy difference in the absence of the Josephson coupling. In Eq. (3) the adiabaticity parameter γ defines whether the development is adiabatic ($\gamma \gg 1$) or sudden ($\gamma \ll 1$).

When the system is coherent, and the degeneracy point is crossed several times, the transition amplitudes for each subsequent pass have to be added for evaluating the transition probability. These amplitudes may be tracked by the ‘scattering’ matrix S , defined by (cf. Refs. [8,23,24,25]):

$$\begin{pmatrix} |-\rangle \\ |+\rangle \end{pmatrix} \Rightarrow \begin{pmatrix} \sqrt{1 - P_{LZ}} \exp(i\tilde{\phi}_S) & i\sqrt{P_{LZ}} \\ i\sqrt{P_{LZ}} & \sqrt{1 - P_{LZ}} \exp(-i\tilde{\phi}_S) \end{pmatrix} \begin{pmatrix} |-\rangle \\ |+\rangle \end{pmatrix}, \quad (4)$$

where phase factors are chosen to simplify the matrix. Here the scattering phase is $\tilde{\phi}_S = \phi_S - \pi/2$, where the Stokes phase ϕ_S depends on the adiabaticity parameter γ :

$$\phi_S = \pi/4 + \arg(\Gamma(1 - i\gamma)) + \gamma(\ln \gamma - 1). \quad (5)$$

In the adiabatic limit, $\tilde{\phi}_S \rightarrow -\pi/2$, while in the sudden limit, $\tilde{\phi}_S = -\pi/4$.

Away from the degeneracy point, the eigenstates $|-\rangle$ and $|+\rangle$ accumulate the relative dynamical phase

$$\varphi_d = \varphi^{(+)} - \varphi^{(-)} = -\frac{1}{\hbar} \int [E_+(n_g(t)) - E_-(n_g(t))] dt. \quad (6)$$

Thus, the condition for constructive interference is that $\varphi_L - 2\tilde{\phi}_S$ and $\varphi_R - 2\tilde{\phi}_S$ are multiples of 2π , where φ_L and φ_R refer to the dynamical phases accumulated on the left and right sides of the degeneracy point, respectively. For example, in the adiabatic limit, $\varphi_{L,R}$ have to be odd multiples of π .

The LZ interference can also be employed to suppress the tunneling to the upper level [26]. In fact, the contrast for destructive interference in the experimental data looks often better than for constructive interference, and these conditions can be employed more simply to determine the behavior of the system as the ground-state response in the measurement is well known. In this case the interference conditions are

$$\varphi_L + 2\pi\ell = 2\phi_S \text{ and } \varphi_R + 2\pi\ell = 2\phi_S \quad (7)$$

with an integer ℓ .

In the sudden limit, $\gamma \ll 1$, the periodically driven two-level system can be solved in a rather straightforward manner [27]. At degeneracy, the probability of being in the upper state varies periodically with time according to

$$P(t) = \sin^2 [B_x J_0(A/\hbar\omega_{rf})\Delta t/\hbar], \quad (8)$$

where J_0 denotes the zeroth Bessel function, and A ($= 4E_c n_g^{\text{rf}}$ below) is the drive amplitude at frequency $f_{\text{rf}} = \omega_{\text{rf}}/2\pi$. One notices that the destruction of tunneling takes place, when the ratio $A/\hbar\omega_{\text{rf}}$ coincides with a zero of J_0 .

The description of interference patterns in a Cooper-pair box using the scattering matrix formalism has been discussed in Refs. [28,29]. In general, relaxation phenomena

should be included as they have strong influence on the sharpness of the interference fringes. For this reason, our main analysis method has been based on spin-1/2 NMR simulations [4,29], which also includes linear response calculations in order to obtain the measured, effective capacitance. Alternatively, the dressed-state approach may be employed as has been done by C. Wilson *et al.* [6].

4 Measurement results on CPB

We have performed low-dissipation microwave reflection measurements [30,31,32] on a series LC resonator in which the box effective capacitance,

$$C_{\text{eff}}^{\pm} = -\frac{\partial^2 E_{\pm}(\phi, n_{\text{g}})}{\partial V_{\text{g}}^2} = -\frac{C_{\text{g}}^2}{e^2} \frac{\partial^2 E_{\pm}(\phi, n_{\text{g}})}{\partial n_{\text{g}}^2},$$

is a part of the total capacitance $C_S + C_{\text{eff}}^{\pm}$, where the superscript \pm refers to ground and excited states of the qubit.¹ The resonator is formed by a surface mount inductor of $L = 160$ nH. With a stray capacitance of $C_S = 250$ fF due to the fairly big lumped resonator, the resonant frequency is $f_0 = 800$ MHz, and the quality factor $Q \simeq 16$ is limited by the external $Z_0 = 50 \Omega$. When C_{eff}^{\pm} varies, the phase and amplitude of the reflected signal $V_{\text{out}} = \Gamma V_{\text{in}}$ change, which is measured by the reflection coefficient $\Gamma = (Z - Z_0)/(Z + Z_0) = \Gamma_0 e^{i \arg(\Gamma)}$. Here, Z is the resonator impedance as seen from the end of the 50Ω coaxial cable used for the reflection measurement. The variation in $\arg(\Gamma)$ due to modulation in C_{eff}^{\pm} is up to 40° in our measurements, corresponding to a shift of resonance frequency $\Delta f_p \simeq 6$ MHz. In all the measurements, the weak probing signal V_{in} at frequency f_m was continuously applied, in addition to the DC-bias and the rf-drive. Thus, the total gate charge variation, in units of e , can be written as $n_{\text{g}}(t) = n_{\text{g}0} + n_{\text{g}}^{\text{rf}} \sin(2\pi f_{\text{rf}} t) + n_{\text{g}}^m \sin(2\pi f_m t)$, where the 1^{st} , 2^{nd} , and 3^{rd} terms correspond to the DC, rf, and measurement drives, respectively.

We have made extensive scans of the CPB reflection by varying the LZ drive frequency $f_{\text{rf}} = 0.1\text{--}20$ GHz and its amplitude $n_{\text{g}}^{\text{rf}} = 0\text{--}3$ electrons, as well as the qubit DC-bias: $n_{\text{g}0}$ and ϕ . In Fig. 3 we present the reflection phase $\arg(\Gamma)$ and magnitude $|\Gamma|$ measured at $f_{\text{rf}} = 4$ GHz on the plane spanned by n_{g}^{rf} and $n_{\text{g}0}$. The Josephson capacitance $C_{\text{eff}} \sim -\arg(\Gamma)C_S^{3/2}Z_0/(2\sqrt{L})$ deduced from the data of Fig. 3 has been given in Ref. [4]². We observe in Fig. 3 a clear interference pattern whose main features confirm the coherent LZ tunneling picture: 1) There is an onset of the interference speckles, where the rf drive just reaches the avoided crossing (charge degeneracy), $n_{\text{g}0} \pm n_{\text{g}}^{\text{rf}} = n_{\text{g,deg}} = \text{odd integer}$, with a linear dependence between $n_{\text{g}0}$ and the AC drive amplitude. Additionally we have shown in Ref. [4] that 2) the density of the dots is proportional to $1/f_{\text{rf}}$ in the direction of $n_{\text{g}0}$ as well as n_{g}^{rf} , and 3) the pattern loses its contrast below a certain drive frequency, in this circuit around $f_{\text{rf}} \sim 2$ GHz.

In Fig. 3a at charge degeneracy, we observe a clear sequence of blue dots that signifies a similar response as in the ground state. These dots correspond to the destruction of tunneling due to periodic rf-drive of our two level system. Note also that these locations correspond to a large reflection magnitude in Fig. 3b. In fact, the reflection is enhanced compared with the undriven level, which indicates transfer of energy from

¹ For a more detailed description of C_{eff} , see Refs. [21,4]

² Full circuit analysis was employed in the evaluation of the reported effective capacitance.

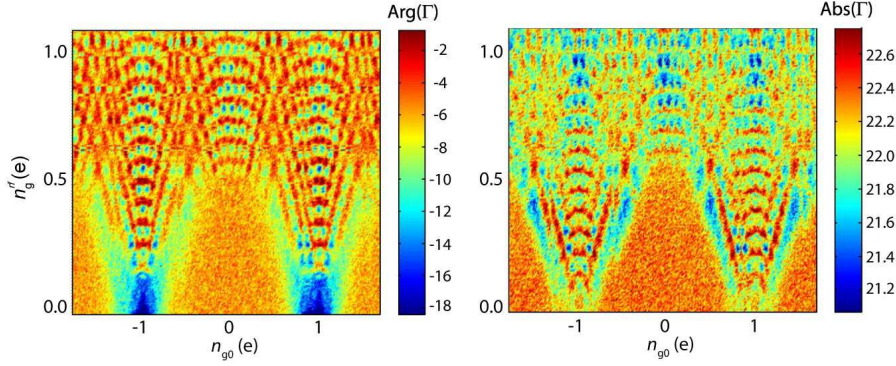


Fig. 3 Reflection phase (left-a) and magnitude (right-b) measured in the configuration of Fig. 1a at rf-drive frequency of $f_{\text{rf}} = 4$ GHz using phase bias $\phi = \pi$, corresponding to the level repulsion of $2\Delta = E_J d = 2.7$ GHz. n_g^{rf} specifies the amplitude of the rf drive in electrons and n_{g0} is the DC charge bias. The vertical bars give the color scales in degrees and dB for the left and right frames, respectively.

the microwave drive, via the qubit, to the resonator. Apparently, the destruction of tunneling prevents the microwave energy from being deposited to the two-level system, and the ‘extra’ energy is dumped out at both drive frequencies.

The order number of the destructive interference dots in Fig. 3 is plotted in Fig. 4. At large rf-drives, the interference dots display a linear dependence on the drive amplitude. The linear dependence is a sign of asymptotic behavior that can be obtained either from Eq. (7) or from Eq. (8). Starting from Eq. (7), we may evaluate $\varphi_{L,R}$ under a drive of $\Delta E = 4E_c n_g^{\text{rf}} \sin(\omega_{\text{rf}} t)$. This yields

$$\varphi_{L,R} = -\frac{8E_c n_g^{\text{rf}}}{\hbar\omega_{\text{rf}}} \mp m\pi + O\left(\frac{\hbar\omega_{\text{rf}}}{4E_c n_g^{\text{rf}}}\right),$$

where m indexes the fringe number, and $\ell_R = \ell_L - m$, where $\ell_{L,R}$ are the integers from Eq. (7). Thus, we find

$$n_g^{\text{rf}} = \frac{\hbar\omega_{\text{rf}}}{8E_c} \left[2\pi\left(\ell_L - \frac{m+1}{2}\right) - 2\tilde{\varphi}_S \right] \quad (9)$$

(note that the order of resonance grows with ℓ_L , and Eq. (9) holds, of course, only for sufficiently large ℓ_L , when it gives $n_g^{\text{rf}} \leq 0$). For the destructive interference at charge degeneracy in the sudden limit this yields $n_g^{\text{rf}} = (2\pi\hbar\omega_{\text{rf}}/8E_c)(\ell_L - \frac{1}{4})$. By fitting Eq. (9) to three/four highest drive points of the data in Fig. 4 we get $\varphi_S/\pi = 0.30 \pm 0.03$, which is close to the theoretical expectation of 0.25. However, there is always an additional contribution from the dynamical phase picked up near the degeneracy point where the bands are curving from linear. This contribution was estimated to be about 1/3 from the expected Stokes phase. This correction will drop the vertical offset, and reduce the Stokes phase down to 0.20π . Hence, taking all the uncertainties into account, our final estimate for the Stokes phase becomes $(0.2 \pm 0.05)\pi$ in the sudden limit.

A fit using the plain dynamic phase of Eq. (6), and the two level approximation for the adiabatic energy levels, is given by the dashed curve in Fig. 4. The x -scale of the

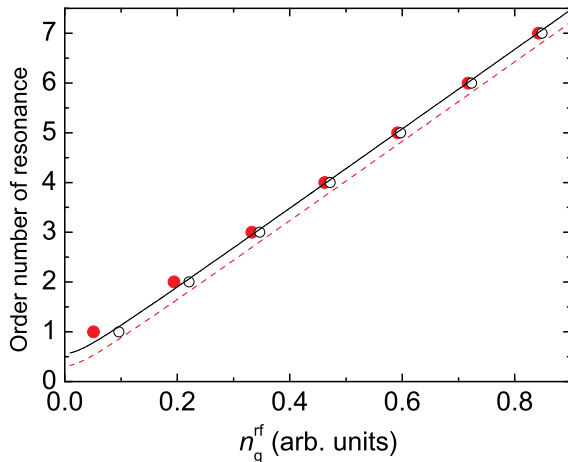


Fig. 4 Order number of destructive interference fringes at charge degeneracy ($n_{g0} = 1$) as a function of the microwave drive amplitude n_g^{rf} for phase bias $\phi = 0$. For comparison, the dynamical phase calculated from Eq. (6) is given by the solid and dashed curves with and without Stokes phase, respectively. The zeroes of Bessel function J_0 are given by the open circles. For details, see text.

calculated curve has been adjusted to match the experimental results at large drive amplitudes. The solid curve, on the other hand, is the dynamical phase corrected using the calculated Stokes phase in the sudden limit. The curve agrees with data except at the lowest points where a possible inaccuracy in the asymmetry parameter has its strongest influence. The open circles display the result of Eq. (8), *i.e.* the zeroes of J_0 , which are also seen to coincide well with the data.

The Stokes phase is related to the non-adiabatic geometric phase, the Aharonov-Anandan phase [33,24]. It is rather straightforward to show that

$$\Phi_{\text{geom}} = 2(1 - P_{LZ})\tilde{\varphi}_S + \pi(1 - m) + \pi P_{LZ}(2m + 2\ell_L - 1). \quad (10)$$

From this relation one gets at the charge degeneracy ($m = 0$): $\Phi_{\text{geom}} = (1 - P_{LZ})(2\tilde{\varphi}_S - \pi(2\ell_L - 1))$, which is nearly the same relation as what we derived for the asymptotic fit in Fig. 4, cf. Eq. (9). Consequently, the geometric Aharonov-Anandan phase could be approximately determined by taking the measured drive amplitude at the point of destructive interference and multiplying the result by $-(8E_c/\hbar\omega_{\text{rf}})(1 - P_{LZ})$. For the data in Fig. 4 at 4 GHz, we get a nearly constant value $(0.20\text{--}0.21) \times 2\pi$ at drive amplitudes around $n_g^{\text{rf}} = 0.5\text{--}1$.

5 Artificial molecule

In the inductive SET, LSET, of Fig. 1b, a stronger coupling between the qubit and the resonator can be achieved than in the Cooper-pair-box configuration. This leads to more involved multiphonon phenomena which are reminiscent of the transitions in diatomic molecules. These transitions can also be viewed as interference effects, and it

is convenient and instructive to describe them as interference in the phase space [13, 34].

In order to understand the molecular analogy, we consider the single-Cooper-pair transistor as a two-state system. The two states are the analog of two electronic states in a diatomic molecule. The transistor is coupled in parallel with an LC oscillator. The LC oscillator is the analog of nuclear vibrations in the molecule. Because of the coupling between the two-state system and the oscillator, a transition between the electronic levels is often accompanied by a change of the vibrational state. Such transitions, where both vibrational and electronic quantum numbers change simultaneously, are known as *vibronic*.

For quantitative analysis, we write the Hamiltonian in the basis of two relevant charge states of the qubit:

$$H(\Phi, q) = \frac{1}{2} \left(\sigma_z E_{\text{el}} - \sigma_x E_J \cos \frac{\pi\Phi}{\Phi_0} + \sigma_y E_J d \sin \frac{\pi\Phi}{\Phi_0} \right) + \frac{q^2}{2C} + \frac{(\Phi - \Phi_b)^2}{2L}. \quad (11)$$

Here the flux Φ and the charge q in the LC oscillator are conjugate variables, and $(\sigma_x, \sigma_y, \sigma_z)$ are the Pauli matrices. The capacitive energy $E_{\text{el}} = 2e^2(n_{g0} - 1)/C_\Sigma$ can be controlled by the gate voltage. Another control parameter is the flux bias Φ_b through the loop containing SCPT and the inductor.

In the following we concentrate on the limit, where the oscillator frequency $1/\sqrt{LC}$ is much lower than the qubit level difference. This means that all changes in the qubit system are much faster than in the oscillator system. Therefore, one can diagonalize the qubit part separately from the oscillator. The two energies of the qubit are obtained by diagonalizing the 2×2 matrix part of Eq. (11):

$$E = \pm \frac{1}{2} \sqrt{E_{\text{el}}^2 + E_J^2 \cos^2 \frac{\pi\Phi}{\Phi_0} + E_J^2 d^2 \sin^2 \frac{\pi\Phi}{\Phi_0}}. \quad (12)$$

This form is valid when the Josephson coupling is a small perturbation compared to the capacitive energy E_{el} . It is also possible to consider the general case of an arbitrary ratio of the Josephson coupling to E_{el} , in which case the energies of the two lowest states are given by Mathieu characteristics. This means that the dependence of the eigenenergies on Φ would be more complicated than in Eq. (12) but otherwise the following analysis remains intact.

Considering now the oscillator, we can think about the capacitive and inductive terms in the Hamiltonian as the kinetic and potential energies. In addition to the inductive potential, there is a potential arising from the qubit, since the qubit energy (12) depends on the flux Φ . Thus there are two potential curves for the oscillations

$$U_{\pm}(\Phi) = \pm \frac{1}{2} \sqrt{E_{\text{el}}^2 + E_J^2 \cos^2 \frac{\pi\Phi}{\Phi_0} + E_J^2 d^2 \sin^2 \frac{\pi\Phi}{\Phi_0}} + \frac{(\Phi - \Phi_b)^2}{2L}. \quad (13)$$

Such a potential is illustrated in Fig. 5a. The different slopes of the qubit energies give rise to a relative shift of the minima of the oscillator potentials. The difference in the curvatures of the qubit energies shifts the vibrational frequencies. Figure 5a, which is drawn to scale with realistic parameters of our circuit, shows that vibronic transitions can be induced by microwave radiation.

The intensities of vibronic transitions are traditionally analyzed in terms of the Franck-Condon principle, and this analysis turns out to be useful for understanding of our data. In its classical form, the Franck-Condon principle says that transitions are

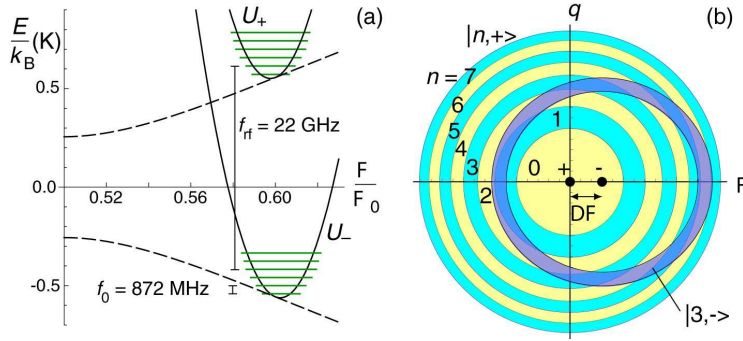


Fig. 5 The potentials and phase-space picture of vibronic transitions. (a) The potentials U_{\pm} (solid curves) for vibrations correspond to two qubit states \pm . The qubit energy (12) is given by dashed lines. The energies of six lowest vibrational states corresponding to both qubit states are drawn. The bars represent energy shifts induced by high and low frequency drives. (b) The overlap of $|+, n\rangle$ states with $n = 0, 1, \dots, 7$ vibrational quanta with state $|-, 3\rangle$ in the phase space. The dots show the centers of the ellipses corresponding to qubit states \pm , which are displaced from each other by $\Delta\Phi$.

possible between vibrational states, the trajectories of which intersect in phase space, and they are most intense between states with coincident turning points. This is based on the idea, already stated, that the transitions between electronic states are fast and the vibrations are slow, so that the vibrational coordinates, here the flux Φ and the charge q , have no time to change during the transition. In addition, $\dot{\Phi}(t)$ is slowest near the turning points, and therefore transitions there are most likely. In the following we discuss how this picture can be extended by semiclassical analysis in phase space, as shown in Refs. [13,34], and how this interpretation is related to the data obtained.

The phase space formed by the coordinate Φ and the canonical momentum q is illustrated in Fig. 5b. The vibrational states correspond to elliptic rings. By scaling the coordinates properly, a state with n vibrational quanta in a harmonic oscillator can be associated with a circular ring between radii \sqrt{n} and $\sqrt{n+1}$ (Planck-Bohr-Sommerfeld bands [34]). This is the case for the upper qubit state in Fig. 5b. Due to a different resonance frequency, the vibrational states corresponding to the lower qubit state then appear as slightly squeezed in the q direction. The shift of the minima of the potentials U_{\pm} (Fig. 5a) appears in the phase space so that the ellipses corresponding to the states $|+, n\rangle$, where $+$ means the upper qubit state, have different centers than the ellipses corresponding to the states $|-, n\rangle$. Vibronic transitions can occur only between states whose ellipses overlap in the phase space. In the example of Fig. 5b, the state $|-, 3\rangle$ has overlap only with states $|+, n\rangle$ with $1 \leq n \leq 6$. In general, the transition rates are determined by the area of the intersection of the respective bands. This area is largest when the ellipses touch each other tangentially, i.e., when the turning points coincide, and this leads to the classical version of the Franck-Condon principle. In the present case though, the overlap consists of two crossings of the ellipses, and one has to add the transition amplitudes taking into account the relative phase accumulated between the crossings. The matrix element of the transitions, $|\langle +, n | - , m \rangle|^2$, is given by the formula [13,34]

$$P_{nm} = \frac{4S_{nm}}{h} \cos^2 \frac{A_{nm}}{\hbar} \quad (14)$$

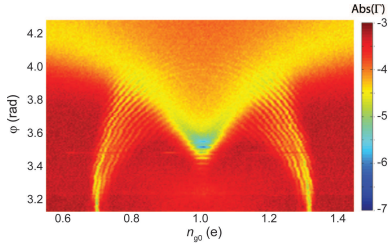


Fig. 6 Measured amplitude $|\Gamma|$ of the reflection coefficient in the bias plane of gate charge n_{g0} and phase $\phi = 2\pi\Phi_b/\Phi_0$. Several concentric circular fringes are visible below the V-shaped light region. Out of them only the pure electronic transition ($n = m$) remains visible at $\phi = \pi$, and corresponds qubit level separation at $f_{\text{rf}} = \Delta E/h = 22$ GHz. The color bar gives the scale for the magnitude of the reflection coefficient in dB. The measurement power was $P_0 = -129$ dBm referred to the coupling capacitor.

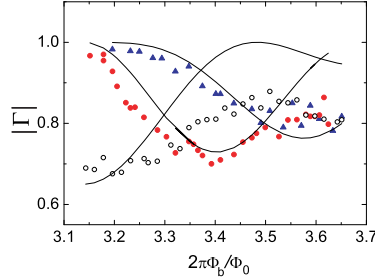


Fig. 7 Variation of reflection coefficient along three fringes in Fig. 6. They correspond to $n - m = 0, -1$, and -2 and are denoted by \circ , \bullet , and \blacktriangle , respectively. The fringe behavior is fitted to Bessel functions J_0^2 , J_1^2 , and J_2^2 . For details, see text.

Here S_{nm} is the area of one of the crossing of the elliptic rings, which sets the maximum probability of the transitions. The phase in the phase factor is determined by the area A_{nm} between the two alternative paths between the crossing points. Eq. (14) reproduces well the results of full quantum calculation except near the classical turning points (where the two crossing areas merge). In the case of Fig. 5 the oscillations are nearly harmonic and the relative difference of frequencies is small. When, in addition, the difference in the vibrational quanta is small, $|n - m| \ll n$, the probability P_{nm} scales as $J_{n-m}^2(2b\sqrt{n})$, where $b = \sqrt{\omega C/2\hbar}\Delta\Phi$ is the dimensionless separation of the potential minima. Owing to the parabolic bands in the region near the minimum gap, $b \propto (\Phi_b/\Phi_0 - 1/2)$, when $|\Phi_b/\Phi_0 - 1/2| \ll 1$.

The measurements on the artificial molecule are made by analyzing the reflection of microwaves at a frequency f_0 close to the resonance frequency f_{LC} of the circuit. In order to induce vibronic transitions, a microwave excitation at frequency f_{rf} was used. The resonance condition for vibronic transition between states $|-, m\rangle$ and $|+, n\rangle$ is

$$f_{\text{rf}} \approx \frac{\Delta E}{h} + (n - m)f_{LC}, \quad (15)$$

where ΔE is the qubit energy splitting. A measurement of reflection coefficient Γ in the bias plane (n_g, Φ_b) is shown in Fig. 6. The vibronic transitions are seen as fringes, making half-circles in the bias plane. The fringes are located within a crescent-shaped area. The language of interference in phase space allows one to easily understand, for instance, the shape of this area, the positions of the fringes and the modulation along the fringes. At $\Phi_b = \Phi_0/2$ only the pure electronic transition is seen. This agrees with the analysis above since there the displacement of the oscillation minima vanishes. With increasing Φ_b more fringes appear, which is in agreement with the growing separation of the minima, and the range of the fringes at a given Φ_b can be determined as in Fig. 5b. In addition, the above picture of enhanced probability of the extremal trajectories is

reflected in the shape of the absorption pattern in Fig. 6, where the edges of the fan-like structure are rather clearly expressed.

The strength of the fringes in the reflection measurement depends on two separate factors. One is the transition probability to the upper qubit state. In large part of the bias plane (below the the V-shaped light region in Fig. 6) the averaged frequency of being part time in the upper and part time in the lower qubit state matches better to the measuring frequency than being in the lower state only. This leads to absorption which is approximately proportional to the transition rate to the upper qubit state. The other factor is the heating or cooling effect caused by the high-frequency f_{rf} radiation on the vibrations. For a vibronic transition with $n > m$ (i.e. $f_{\text{rf}} > \Delta E/\hbar$), the resonance deposits energy into the resonator causing heating of the vibrations. This leads to decreased absorption of the measurement wave. In the opposite case $n < m$, the absorption of a high frequency photon cools the oscillator by reducing its quanta which leads to increased absorption of the measurement wave. This asymmetry of the fringes is clearly visible in Fig. 6, where the cooling fringes at larger radii are stronger than the heating fringes at smaller radii.

Numerical simulations of the artificial molecule has been done in Ref. [12]. These are based on Bloch equations describing the qubit and classical equations describing the circuit. They reproduce well the observed vibronic spectrum, both the matrix elements and the heating/cooling asymmetry. Here we present a simplified analysis by comparing three of the fringes with the transition probability $P_{nm} = J_{n-m}^2(2b\sqrt{n})$, neglecting the heating/cooling effect. Fig. 7 displays the measured reflection magnitude along fringes with $n - m = 0, -1$, and -2 as a function of the flux bias of the qubit. Squared Bessel functions J_0^2 , J_1^2 , and J_2^2 have been fitted to the data. For the x -scale argument we have taken $\text{const} \times (\Phi_b/\Phi_0 - 1/2)$ although this approximation will be rather crude when $\Phi_b/\Phi_0 > 0.54$. Nevertheless, the comparison can be employed to look for the presence of basic interference phenomena. The agreement between the data and the fits is quite good, though the modulation of the pure electronic fringe is a bit weaker in the measurement than given by J_0^2 .

The reason for smearing of the Bessel modulation is the variation of the number of quanta in the resonator. Assuming the resonator is in a coherent state, it is a superposition of the number states and this should be taken into account in the analysis of the interference fringes. This diminishes the sharpest features of the interference, but does not remove it. Consequently, we may conclude that the dip at $\Phi_b/\Phi_0 \approx 0.54$ in the fringe magnitude corresponding to the pure electronic transition, is due to destructive interference in phase space in formula Eq. (14).

In summary, we have discussed interband transitions in superconducting Cooper-pair boxes and charge-phase qubits and argued, how interference effects in various forms can be found to underlie the observed phenomena.

Acknowledgments

Fruitful discussions with M. Feigelman, T. Heikkilä, F. Hekking, and M. Paalanen are gratefully acknowledged.

References

1. A.V. Shytov, D.A. Ivanov, M.V. Feigel'man, European Physical Journal B **36**, 263 (2003)

2. S.N. Shevchenko, A.S. Kiyko, A. Omelyanchouk, W. Krech, *Low Temperature Physics* **31**, 569 (2005), cond-mat/0412588
3. W. Oliver, Y. Yu, J. Lee, K. Berggren, L. Levitov, T. Orlando, *Science* **310**(1653) (2005)
4. M. Sillanpää, T. Lehtinen, A. Paila, Y. Makhlin, P. Hakonen, *Physical Review Letters* **96**(18), 187002 (2006)
5. D.M. Berns, W.D. Oliver, S.O. Valenzuela, A.V. Shytov, K.K. Berggren, L.S. Levitov, T.P. Orlando, *Physical Review Letters* **97**(15), 150502 (2006)
6. C.M. Wilson, T. Duty, F. Persson, M. Sandberg, G. Johansson, P. Delsing, *Physical Review Letters* **98**(25), 257003 (2007)
7. L. Landau, *Phys. Z. Sowjet.* **2**, 46 (1932)
8. C. Zener, *Proceedings of Royal Society (London) A* **137**, 696 (1932)
9. E.C.G. Stueckelberg, *Helv. Phys. Acta* **5**, 369 (1932)
10. Y. Ji, Y. Chung, D. Sprinzak, M. Heiblum, D. Mahalu, H. Shtrikman, *Nature* **422**, 415 (2003)
11. E. Majorana, *Nuovo Cimento* **9**, 43 (1932)
12. D. Gunnarsson, J. Tuorila, A. Paila, J. Sarkar, E. Thuneberg, Y. Makhlin, P. Hakonen, *Physical Review Letters*, **101**, 256806 (2008)
13. J.A. Wheeler, *Letters in Mathematical Physics* **10**, 201 (1985)
14. A. Wallraff, D. Schuster, L.F. A. Blais, R.S. Huang, J. Majer, S. Kumar, S.M. Girvin, R.J. Schoelkopf, *Nature* **431**, 162 (2005)
15. Y. Nakamura, Yu.A. Pashkin, J.S. Tsai, *Physical Review Letters* **87**, 246601 (2001)
16. S. Saito, M. Thorwart, H. Tanaka, M. Ueda, H. Nakano, K. Semba, H. Takayanagi, *Physical Review Letters* **93**(3), 037001 (2004)
17. C.K. Law, *Physical Review Letters* **73**(14), 1931 (1994)
18. V. Bouchiat, D. Vion, P. Joyez, D. Esteve, M.H. Devoret, *Physica Scripta* **T76**, 165 (1998)
19. Y. Nakamura, Yu.A. Pashkin, J.S. Tsai, *Nature* **398**, 786 (1999)
20. Yu. Makhlin, G. Schön, A. Shnirman, *Rev. Mod. Phys.* **73**, 357 (2001)
21. M.A. Sillanpää, T. Lehtinen, A. Paila, Y. Makhlin, L. Roschier, P.J. Hakonen, *Physical Review Letters* **95**(20), 206806 (2005)
22. T. Duty, G. Johansson, K. Bladh, D. Gunnarsson, C. Wilson, P. Delsing, *Physical Review Letters* **95**(20), 206807 (2005)
23. E. Shimshoni, Y. Gefen, *Annals of Physics* **210**, 16 (1991)
24. Y. Kayanuma, *Physical Review A* **55**, R2495 (1997)
25. M. Wubs, K. Saito, S. Kohler, Y. Kayanuma, P. Hänggi, *New Journal of Physics* **7**(218) (2005)
26. F. Grossmann, T. Dittrich, P. Jung, P. Hänggi, *Physical Review Letters* **67**, 516 (1991)
27. Y. Kayanuma, *Physical Review A* **50**(1), 843 (1994)
28. M. Sillanpää, T. Lehtinen, A. Paila, Y. Makhlin, P.J. Hakonen, *Journal of Low Temperature Physics* **146**, 253 (2007)
29. A. Paila, M. Sillanpää, D. Gunnarsson, Y. Makhlin, P. Hakonen, *NANOPHYSICS - From fundamentals to applications* (The Gioi, 2007)
30. M.A. Sillanpää, L. Roschier, P. Hakonen, *Physical Review Letters* **93**, 066805 (2004)
31. L. Roschier, M. Sillanpää, P. Hakonen, *Physical Review B* **71**, 024530 (2005)
32. M.A. Sillanpää, *Quantum device applications of mesoscopic superconductivity*. Ph.D. thesis, Helsinki University of Technology (2005)
33. Y. Aharonov, J. Anandan, *Physical Review Letters* **58**(16), 1593 (1987)
34. W. Schleich, *Quantum Optics in Phase Space* (Wiley-VCH, 2001)